

A multi-wavelength interferometric study of the massive young stellar object IRAS 13481-6124[★]

Paul A. Boley^{1,2}, Stefan Kraus³, Willem-Jan de Wit⁴, Hendrik Linz⁵, Roy van Boekel⁵, Thomas Henning⁵, Sylvestre Lacour^{6,7}, John D. Monnier⁸, Bringfried Stecklum⁹, and Peter G. Tuthill⁷

¹ Ural Federal University, Kourovka Astronomical Observatory, 51 Lenin Ave., Ekaterinburg 620075, Russia

² Max Planck Institute for Radio Astronomy, Auf dem Hügel 69, Bonn 53121, Germany

³ University of Exeter, Astrophysics Group, Stocker Road, Exeter, EX4 4QL, United Kingdom

⁴ European Southern Observatory, Casilla 19001, Santiago 19, Chile

⁵ Max Planck Institute for Astronomy, Königstuhl 17, Heidelberg 69117, Germany

⁶ LESIA/Observatoire de Paris, CNRS, UPMC, Université Paris Diderot, 5 place Jules Janssen, 92195 Meudon, France

⁷ Sydney Institute of Astronomy, School of Physics, University of Sydney, NSW 2006, Australia

⁸ Department of Astronomy, University of Michigan, 830 Dennison Building, 500 Church St., Ann Arbor, MI 48109, United States

⁹ Thüringer Landessternwarte Tautenburg, Sternwarte 5, 07778, Tautenburg, Germany

October 8, 2018

ABSTRACT

We present new mid-infrared interferometric observations of the massive young stellar object IRAS 13481-6124, using VLTI/MIDI for spectrally-resolved, long-baseline measurements (projected baselines up to ~ 120 m) and GSO/T-ReCS for aperture-masking interferometry in five narrow-band filters (projected baselines of $\sim 1.8 - 6.4$ m) in the wavelength range of $7.5 - 13 \mu\text{m}$. We combine these measurements with previously-published interferometric observations in the K and N bands in order to assemble the largest collection of infrared interferometric observations for a massive YSO to date. Using a combination of geometric and radiative-transfer models, we confirm the detection at mid-infrared wavelengths of the disk previously inferred from near-infrared observations. We show that the outflow cavity is also detected at both near- and mid-infrared wavelengths, and in fact dominates the mid-infrared emission in terms of total flux. For the disk, we derive the inner radius (~ 1.8 mas or ~ 6.5 AU at 3.6 kpc), temperature at the inner rim (~ 1760 K), inclination ($\sim 48^\circ$) and position angle ($\sim 107^\circ$). We determine that the mass of the disk cannot be constrained without high-resolution observations in the (sub-)millimeter regime or observations of the disk kinematics, and could be anywhere from $\sim 10^{-3}$ to $20 M_\odot$. Finally, we discuss the prospects of interpreting the spectral energy distributions of deeply-embedded massive YSOs, and warn against attempting to infer disk properties from the SED.

Key words. stars: massive - techniques: interferometric - stars: individual: IRAS 13481-6124

1. Introduction

Studies of the formation processes of massive stars have been strongly limited by the difficulty of observing these objects at early stages. The best evidence for an AU-scale disk around an accreting, massive young star is delivered by the source IRAS 13481-6124. This bright infrared source was first identified as a young stellar object (YSO) by Persson & Campbell (1987), and specifically as a massive YSO by Chan et al. (1996), based on the flux densities measured with the IRAS satellite. Kinematic distance estimates (which are typically only accurate to within about a factor of 2; Xu et al. 2006) to this object range from 3.1 to 3.8 kpc (e.g. Busfield et al. 2006; Urquhart et al. 2007), and no other distance measures are available; thus, as is often the case with such objects, the distance is poorly known. For the present study, we adopt a distance of 3.6 kpc, which Fontani et al. (2005) determined kinematically from observations of rotational transitions of CS and C^{17}O . Scaling the infrared luminosity of $1.8 \times 10^5 L_\odot$ determined by Beck et al.

(1991) to this distance yields a luminosity of $\sim 7.7 \times 10^4 L_\odot$ for IRAS 13481-6124.

Observations of hydrogen recombination lines at near-infrared wavelengths by Beck et al. (1991) showed the presence of an ionizing wind associated with IRAS 13481-6124. From the $\text{Br}\gamma/\text{P}\gamma$ line ratio, these authors estimated a visual extinction of $A_V = 24$ mag, indicating that the source is fairly deeply embedded. Interestingly, several searches for masers (e.g. Scalise et al. 1989; MacLeod et al. 1998), which are often found in regions of massive star formation, failed to reveal any maser emission associated with the source. Beltrán et al. (2006) mapped the continuum emission at 1.2 mm in the region, suggesting an envelope mass (gas + dust) of $1470 M_\odot$ (for a distance of 3.6 kpc).

Mid-infrared spectropolarimetric observations by Wright et al. (2008) revealed the presence of a sharp absorption feature at $11.2 \mu\text{m}$ in the linear polarization spectrum. To date, this feature has only been observed in one other source (AFGL 2591; Aitken et al. 1988), and both Aitken et al. (1988) and Wright et al. (2008) interpret the feature as possibly arising from the presence of crystalline olivine, which could form as a result of dust processing in the circumstellar environment. The apparent rarity of this feature, as noted by Wright et al. (2008), could indicate that IRAS 13481-6124 is currently in a very

[★] Based in part on observations with the Very Large Telescope Interferometer of the European Southern Observatory, under program IDs 384.C-0625, 086.C-0543, 091.C-0357.

short-lived phase of the evolutionary sequence of massive star formation. We note, however, that alternative explanations could be that this feature only occurs if the source has a particular geometry, or if viewed under particular inclination angles.

Interferometric measurements of the source at near-infrared wavelengths were performed by Kraus et al. (2010). The K -band ($\lambda = 2.2 \mu\text{m}$) image reconstructed from these interferometric observations shows an elongated structure, which is oriented perpendicular to the large-scale outflow seen in Spitzer Space Telescope images from the GLIMPSE survey (Churchwell et al. 2009), and more clearly in the continuum-subtracted H_2 images ($\lambda = 2.122 \mu\text{m}$) presented by Caratti o Garatti et al. (2015). Spatially-resolved Q -band ($\lambda = 20 \mu\text{m}$) imaging by Wheelwright et al. (2012) shows an elongated structure roughly along the outflow direction. Radiative transfer modeling of the spectral energy distribution (SED) and near-infrared interferometric data by Kraus et al. (2010) suggest that IRAS 13481-6124 hosts a circumstellar disk, and suggest a total luminosity of $4 \times 10^4 L_\odot$ (i.e., about half the value derived from the IRAS measurements by Beck et al. 1991).

Most recently, K -band integral-field spectroscopic measurements by Stecklum et al. (2012) showed a photocenter shift of ~ 1 AU in the $\text{Br}\gamma$ line along the same position angle as the bow shock reported by Kraus et al. (2010), which confirms the association of the parsec-scale outflow with the MYSO. Furthermore, these integral-field measurements also show evidence for (possibly non-Keplerian) rotation perpendicular to the outflow direction, providing yet another indication of a circumstellar disk in this system.

In this work, we consider the K -band and N -band ($\lambda = 8 - 13 \mu\text{m}$) interferometric measurements presented by Kraus et al. (2010) and Boley et al. (2013), respectively, together with new N -band interferometric measurements of the source, obtained using both long-baseline and aperture-masking interferometry. We use geometric models of the near-/mid-infrared interferometric observations, and probe the source on spatial scales (given by $\sim \lambda/2B$, where λ is the wavelength, and B is the projected baseline of the interferometric observations) of about 10–1000 AU. We focus on the wavelength behavior of the fits, which we examine in the context of the temperature profile of the circumstellar disk.

2. Observations

2.1. Long-baseline interferometry with VLTI

New observations of IRAS 13481-6124 were conducted in the N band ($8-13 \mu\text{m}$) using the mid-infrared interferometric instrument MIDI (Leinert et al. 2003) at the Very Large Telescope Interferometer (VLTI) of the European Southern Observatory (ESO) in 2010–2013. The MIDI instrument is a two-telescope beam combiner which measures spectrally-dispersed correlated and total flux, with either a grism ($\lambda/\Delta\lambda \approx 230$) or a prism ($\lambda/\Delta\lambda \approx 30$) serving as the dispersive element. Using MIDI, light can be combined simultaneously from either two of the 8-m Unit Telescopes (UTs) or two of the 1.8-m Auxiliary Telescopes (ATs).

The observations presented in this paper were taken in the HIGHSENS mode, meaning the correlated and total flux measurements are made separately. We summarize the interferometric measurements in Table 1, where we show the time the fringe track was started, the telescopes/interferometric stations used, the projected baseline and position angle, as well as the average visibility, dispersive element and ESO program ID. Each

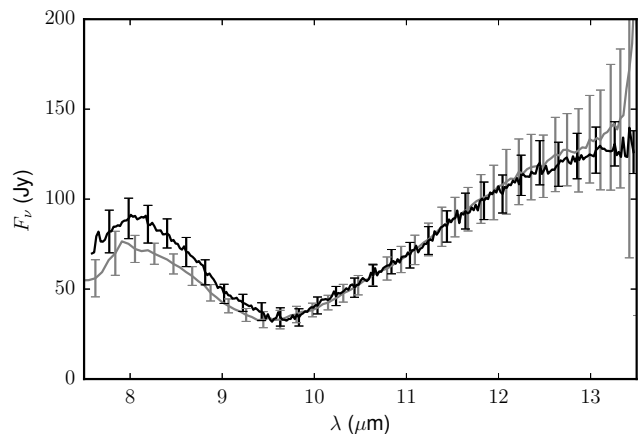


Fig. 2. Total N -band spectrum of IRAS 13481-6124. The gray line shows the spectrum observed with the prism (Boley et al. 2013); the black line shows the spectrum measured with the grism.

interferometric measurement was preceded and/or followed by a calibration measurement of a bright star of known brightness and diameter, taken from the van Boekel mid-infrared calibrator star database (van Boekel 2004). The observations in 2013 were obtained using the UTs with the grism as the dispersive element, while the observations in 2010–2012 used the ATs and the lower-resolution prism.

Data reduction was performed using version 2.0Beta1 (8 Nov. 2011) of the MIA+EWS package (Jaffe 2004). We used the fringe pattern of the individual calibrator stars to create a median mask for each night/baseline configuration, which was then used for extracting the correlated flux from the science measurements. Calibrated correlated fluxes (in Jy) were computed using the measurements of the calibrator stars, and the uncertainty in the correlated flux was taken as the root-mean-square sum of the random error derived from MIA+EWS and the systematic error derived from the calibrator measurements.

Finally, we also make use of the 36 MIDI observations presented as part of the VLTI/MIDI MYSO Survey (Boley et al. 2013). The observations presented in that work were reduced in an identical fashion as in the present work. The projected baselines of this combined MIDI data set range from ~ 9 to ~ 128 m; we show the resulting uv coverage in the right-hand panel of Fig. 1. As in the work by Boley et al. (2013), we derive spectrally-dispersed visibilities from the correlated fluxes by dividing the correlated flux spectra by the median spectrum measured with the UTs. For the observations with the prism, we use the same total spectrum (also obtained with the prism) as Boley et al. (2013); for the observations with the grism, we use the median of the total flux spectra obtained with the grism on 2013-04-30 and 2013-05-01 (see Fig. 2). OIFITS files of the MIDI data are available upon request.

2.2. Aperture-masking interferometry with Gemini-South

Short-baseline interferometric observations of IRAS 13481-6124 were also performed using the aperture-masking technique implemented at the Thermal-Region Camera Spectrograph (T-ReCS; De Buizer & Fisher 2005) at the Gemini South Observatory (GSO) on May 7, 2007 (program ID GS-2007A-Q-38). This technique works by apodizing the pupil with a mask with several holes in it, thus transforming the single large telescope mirror into an array of smaller sub-apertures. Images formed are

Table 1. Log of new MIDI observations of IRAS 13481-6124

Date/time (UTC)	Telescopes	Proj. baseline (m)	Position angle (deg.)	Avg. visibility	Dispersive element	Program ID
2010-02-14 08:39	E0-G0	15.8	71.0	0.42	PRISM	384.C-0625(A)
2011-03-11 03:55	G1-I1	44.8	9.4	0.20	PRISM	086.C-0543(B)
2011-03-11 04:06	G1-I1	44.7	11.5	0.20	PRISM	086.C-0543(B)
2011-03-11 05:28	G1-H0	57.8	174.7	0.15	PRISM	086.C-0543(B)
2011-03-11 07:49	D0-I1	82.3	104.8	0.09	PRISM	086.C-0543(B)
2011-03-11 08:28	H0-I1	36.3	155.2	0.21	PRISM	086.C-0543(A)
2011-03-13 05:51	G1-K0	79.3	19.0	0.13	PRISM	086.C-0543(C)
2011-03-31 04:52	D0-I1	79.9	83.2	0.09	PRISM	086.C-0543(B)
2011-03-31 06:16	D0-I1	82.1	101.5	0.08	PRISM	086.C-0543(B)
2011-05-03 05:44	G1-I1	36.4	66.9	0.22	PRISM	086.C-0543(A)
2012-02-24 06:42	D0-I1	78.5	76.6	0.12	PRISM	086.C-0543(C)
2012-03-29 02:53	A1-I1	102.4	41.3	0.14	PRISM	086.C-0543(A)
2012-03-29 03:03	A1-I1	102.8	43.6	0.12	PRISM	086.C-0543(A)
2012-04-01 07:00	A1-I1	104.5	100.1	0.09	PRISM	086.C-0543(A)
2012-04-01 09:02	G1-K0	59.7	60.2	0.18	PRISM	086.C-0543(C)
2012-04-01 09:11	G1-K0	58.6	61.6	0.18	PRISM	086.C-0543(C)
2013-04-30 04:13	UT1-UT4	123.3	68.3	0.06	GRISM	091.C-0357(B)
2013-04-30 04:27	UT1-UT4	122.1	71.3	0.06	GRISM	091.C-0357(B)
2013-05-01 06:21	UT2-UT3	34.5	72.8	0.20	GRISM	091.C-0357(A)

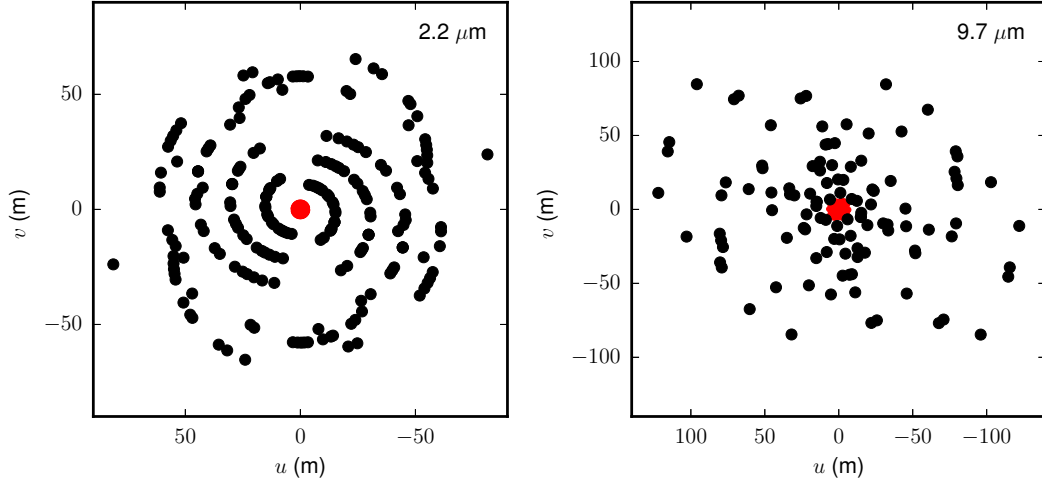


Fig. 1. uv coverage of the interferometric measurements. The left panel shows the coverage of the near-infrared measurements, while the right panel shows the coverage of the mid-infrared measurements. Black points show the long-baseline VLTI observations (AMBER and MIDI), while the speckle-interferometry and aperture-masking observations (NTT and GSO/T-ReCS) are shown in red.

now Fizeau interference patterns, and the complex visibilities corresponding to each baseline passed by the mask may now be extracted using Fourier transform techniques. Further details of this technique are described by Tuthill et al. (2000), while an interesting adaptation of the technique to mid-infrared interferometric data is given by Monnier et al. (2004). A recent example of the application of this technique can be found in the work of Vehoff et al. (2010), who used T-ReCS observations similar to those presented here to reconstruct a diffraction-limited image at a wavelength of $11.7 \mu\text{m}$ of the MYSO NGC 3603 IRS 9A.

A set of rapid exposures with a total on-source integration time of 131 s were performed in the five narrow-band filters Si1, Si2, Si3, Si5 and Si6, which have central wavelengths of 7.7, 8.7, 9.7, 11.7 and $12.4 \mu\text{m}$, respectively, and widths in the range of $\sim 0.7\text{--}1.2 \mu\text{m}$ (bandpasses overplotted in Fig. 3). The raw visibility quantities extracted (V^2 and closure phase) are cali-

brated for the effects of the telescope-atmosphere transfer function with the use of contemporaneous observations of a nearby point-source reference star. The aperture-masking observations presented here measure the visibility amplitude with projected baselines of 1.8–6.4 m; the Fourier coverage in the uv plane is concentrated in the red core of the right panel of Fig. 1. The closure phases (not presented in this work) were generally small ($\lesssim 10^\circ$), as expected from a predominantly point-symmetric object. OIFITS files of the T-ReCS observations are available upon request.

2.3. Previously-published K -band observations

IRAS 13481-6124 was observed in the K band with the three-telescope interferometric instrument AMBER at the VLTI in 2008–2009 (program IDs 081.C-0272, 083.C-0236,

PI G. Weigelt; 083.C-0621, PI S. Kraus), and speckle-interferometry observations were made with the 3.6 m ESO New Technology Telescope (NTT) on February 3, 2009 (program ID 082.C-0223, PI S. Kraus). These data were presented by Kraus et al. (2010), and we refer to that publication for further details about the observations and data reduction, however we reiterate the most relevant characteristics of the data here.

The projected baselines of the AMBER measurements range from 11 to 85 m, while the NTT bispectrum speckle measurements provide projected baselines up to ~ 3 m. The AMBER data consist of spectrally-resolved visibility amplitudes and closure phases across the K band ($1.95\text{--}2.55\ \mu\text{m}$) with a spectral resolution $\lambda/\Delta\lambda \approx 35$, while the NTT speckle data consist of just visibility amplitudes at the center of the K band ($2.2\ \mu\text{m}$). We show the uv coverage in the left panel of Fig. 1, where the VLT/AMBER measurements are shown in black, and the NTT speckle data are shown in red.

3. Results

The results of the MIDI and T-ReCS observations are shown in Fig. 3. In the top left panel, as a black line, we show the total N -band spectrum of the source together with the transmission curves of the five filters used for the T-ReCS observations, overlaid in gray. The spectrally-resolved MIDI visibilities were averaged over these filter curves to create values which are directly comparable to the T-ReCS measurements. The remaining five panels of Fig. 3 show the visibility amplitude V as a function of spatial frequency $\nu = B/\lambda$ in each of the five filters, where the T-ReCS data are shown as circles, and the MIDI data are shown as triangles; the color of each data point shows the position angle (measured east of north) of the measurement. **The increased level of noise seen in the observations at $\lambda = 7.7\ \mu\text{m}$ is due to the much lower atmospheric transmission at this wavelength, which is near the edge of the N band.**

First, we note that the transition from the visibilities measured with MIDI to those measured with T-ReCS is smooth and continuous. This confirms that the absolute calibration between these two very different techniques and instruments is consistent, and that the long-baseline observations are directly comparable to those obtained with the aperture-masking technique.

Second, the dependence of the visibility on baseline and wavelength shows that the infrared emission can be approximately described by two components: an extended component causes the visibility to drop quickly at short baselines (spatial frequencies $\lesssim 10$ cycles/arcsec), and a compact component then makes the visibility curve flatten off and decrease more slowly towards longer baselines. The spatial frequency at which the visibility curve flattens is a measure of the size of the extended component, and the visibility amplitude at this point equals the fraction of the total flux that is contributed by the compact component.

Finally, a distinct emission feature was noted at $\sim 11.2\ \mu\text{m}$ in the N -band spectrum of polarized light taken with TIMMI2 (Wright et al. 2008). We note in passing that our MIDI data show no obvious feature at this wavelength, neither in the visibilities nor in the correlated fluxes. This specifically includes the few GRISM data points, which have a higher spectral resolution.

4. Analysis

In this section, in order to perform a reliable analysis of the infrared interferometric observations, we use a series of

progressively-complicated approaches to analyze the data. First, we evaluate our assumptions about the near- and mid-infrared dust extinction in Sec. 4.1. We follow this with geometric fits to the visibilities in Sec. 4.2. Finally, in Sec. 4.3, we elaborate on this approach to include the flux information contained in the mid-infrared observations, both for geometric models (Sec. 4.3.1) and for radiative transfer models (Sec. 4.3.2).

4.1. Near- and mid-infrared extinction

IRAS 13481-6124, like most MYSOs, is heavily affected by extinction. Using the ratio of the Br γ and Pf γ Hydrogen emission lines, Beck et al. (1991) estimated a total (visual) extinction of $A_V \approx 24$ mag for this source. The deep silicate absorption feature seen in the total N -band spectrum (Fig. 2) further attests to the high amount of extinction towards the object, even at mid-infrared wavelengths.

Since we are considering observations at near- and mid-infrared wavelengths in this work, it is necessary to consider the extinction over a wavelength range of $\sim 1\text{--}13\ \mu\text{m}$ – a range for which it has traditionally been very difficult to characterize extinction laws (see, for example, the discussions by Lutz (1999) and Fritz et al. (2011)). We find that the shape of the silicate feature in this object is poorly reproduced by the synthetic extinction curves of Weingartner & Draine (2001) and the empirical extinction curve of Fritz et al. (2011). However, using opacities for amorphous silicates measured in the laboratory by Dorschner et al. (1995), Boley et al. (2013) showed that the absorption feature in the N -band correlated flux spectra of IRAS 13481-6124 is well-reproduced by a mixture consisting primarily of “small” grains ($r = 0.1\ \mu\text{m}$) of pyroxene glass (in the form of MgFeSiO_3) and olivine glass (in the form of MgFeSiO_4), with relative mass abundances of 63% and 36%, respectively, and less than 1% of the mass in “large” ($r = 1.5\ \mu\text{m}$) grains. Furthermore, it was also shown in this work that the shape of the absorption feature in the correlated flux spectra is independent of the spatial scale probed, on projected baselines from 9 to 128 m.

These results from Boley et al. (2013) characterize the contribution of silicates to the line-of-sight extinction in this particular object, however they cannot provide an estimate of the contribution from carbonaceous grain species, which can contribute significantly (or even dominantly, depending on wavelength) to the continuum opacities in interstellar extinction laws. Furthermore, due to the lack of any strong features from most types of carbonaceous species at infrared wavelengths, it is essentially impossible to directly constrain this important dust component for deeply-embedded objects using conventional methods.

As we cannot measure this contribution from carbonaceous grains directly, a reasonable approach to estimate the total foreground extinction towards IRAS 13481-6124 is to simply *adapt* the contribution of carbonaceous grains from a synthetic extinction curve, and combine this with the determination of the silicate component by Boley et al. (2013). In Fig. 4, we show the extinction optical depth $\tau_\nu(\lambda)$ thus derived, where we have taken the same carbonaceous mixture used by Weingartner & Draine (2001) (i.e., graphite grains from Laor & Draine (1993) and PAH grains from Li & Draine (2001)). We used the Milky-Way size distribution from Weingartner & Draine (2001), with two sets of parameters from Table 1 of that work, describing the $R_V = 3.1$ ($b_C = 60$ ppm) and $R_V = 5.5$ ($b_C = 30$ ppm, case “A”) extinction laws. For comparison, we also show the optical depth derived using instead the graphite grains of Li & Draine (2001) with the often-used “MRN” ($dn \propto a^{-3.5} da$, $a_{\min} = 5$ nm,

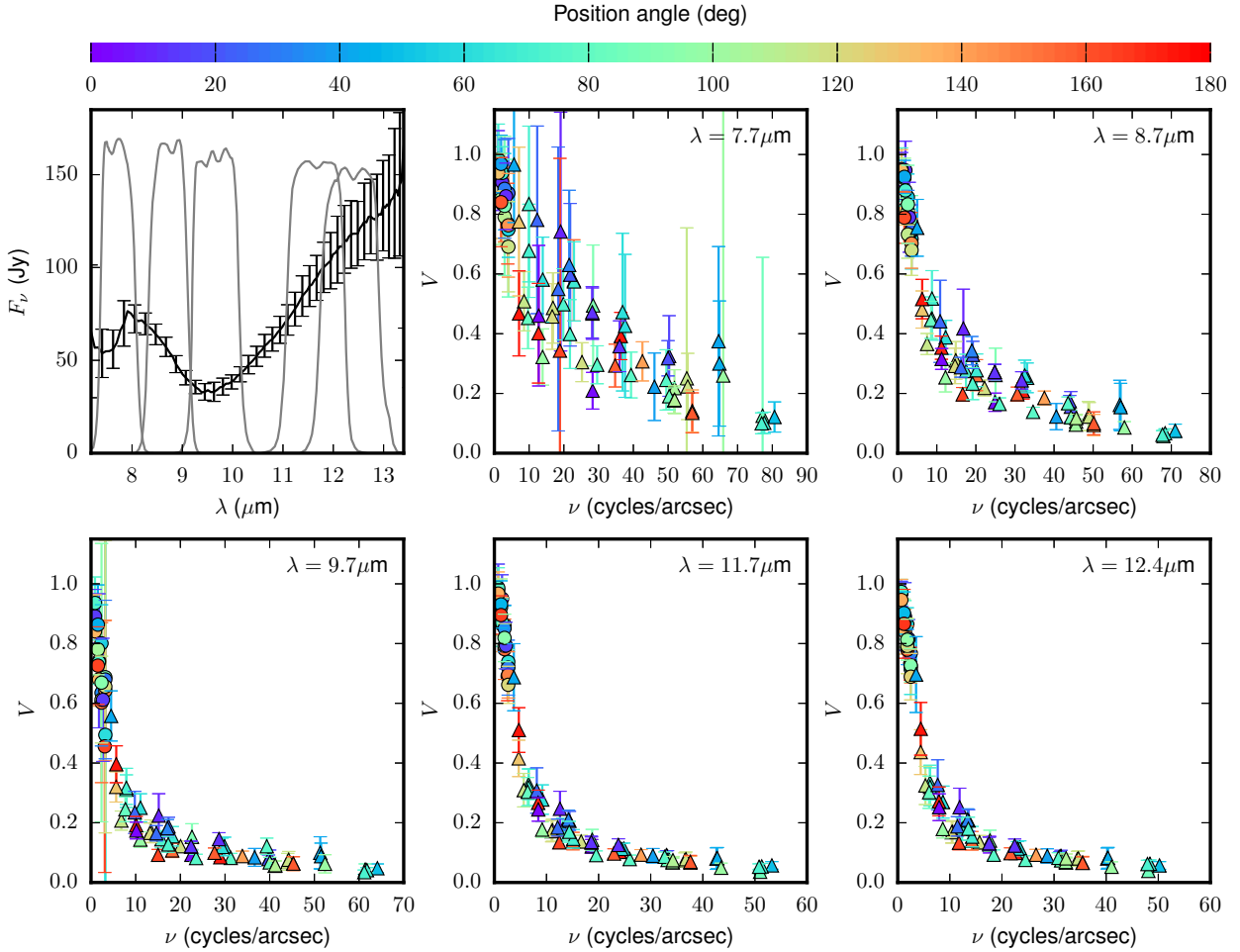


Fig. 3. *Top left panel:* Total N -band spectrum observed with MIDI (black) and the transmission curves for the five filters used for the T-ReCS aperture-masking measurements. *Remaining panels:* The visibility amplitude V as a function of spatial frequency ν in each of the five filters. The T-ReCS measurements are shown as circles, while the MIDI measurements, averaged over each corresponding filter, are shown as triangles. The color of each data point shows the position angle (measured east of north).

$a_{\text{max}} = 250 \text{ nm}$; Mathis et al. 1977) size distribution and a mass ratio of silicates to graphite of 60:40, as well as the $R_V = 3.1$ and $R_V = 5.5$ Milky-Way synthetic extinction curves from Weingartner & Draine (2001).

We note that while the three different extinction curves we derive show essentially identical values for τ_ν in the N -band (inset of Fig. 4), the scatter between all three curves at near-infrared wavelengths is large. Furthermore, at near-infrared wavelengths τ_ν is significantly larger than unity. In terms of magnitudes of extinction ($A_\lambda = 2.5 \log_{10}(e)\tau_\nu(\lambda)$), A_K ranges from 1.8 to 3.1 mag, and A_J ranges from 4.0 to 10 mag. This is of particular importance, as it implies that the derived extinction at near-infrared wavelengths is highly uncertain, and that reliable dereddened flux levels (which scale as $e^{\tau_\nu(\lambda)}$) can not be obtained at these wavelengths. This matter is addressed in more detail in Section 5.3.

4.2. Model fits to the visibilities

As noted in Section 3, the observed visibilities of IRAS 13481-6124 show evidence for two distinct components. Kraus et al. (2010) examined the K -band AMBER/NTT visibilities in terms of several types of two-component geometric models, all of which included an extended, one-dimensional Gaussian “halo”

as one component; the second (two-dimensional) component was either a uniform disk, a thin ring, a compact Gaussian, or a temperature-gradient disk model¹. In the following subsections, we further explore the geometry of the system in the context of the additional information provided by the mid-infrared observations.

4.2.1. Gaussian models

As the Gaussian model provides good fits to the near-infrared data, has fewer parameters than the parameterized disk model, and is conceptually very simple, we begin with this type of model to examine the entirety of the interferometric data. Specifically, we fit the “2D1D” model from Boley et al. (2013) to each wavelength separately; this model consists of a two-dimensional Gaussian (characterized by a full-width-at-half-maximum size $\text{FWHM}_{2\text{D}}$, position angle ϕ and inclination angle i) and a one-dimensional Gaussian (size $\text{FWHM}_{1\text{D}}$), both centered at the origin. The flux ratio between these two components is given by $F_{2\text{D}}/F_{1\text{D}}$. The best-fit parameters were derived with a grid search followed by a downhill-simplex minimization of χ^2 ; uncertain-

¹ See Appendix A for a correction to the geometric fits presented by Kraus et al. (2010).

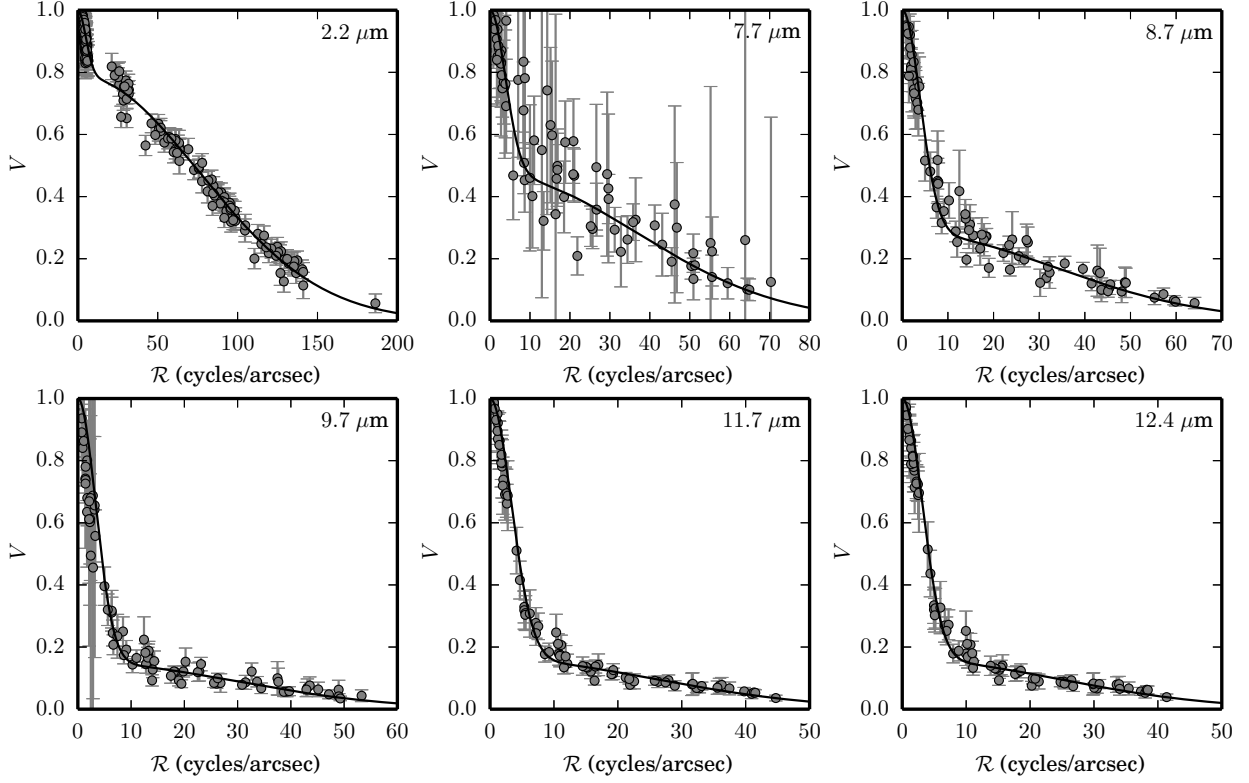


Fig. 5. Gaussian model fits to the visibilities at each wavelength, plotted as a function of deprojected spatial frequency. See Table 2 for the fit parameters. Circles and error bars mark the observations; while the model fits to each wavelength are shown as a solid curve.

Table 2. Fit parameters for 2D1D model

Wavelength (μm)	$F_{2\text{D}}/F_{1\text{D}}$	$\text{FWHM}_{2\text{D}}$ (mas)	$\text{FWHM}_{1\text{D}}$ (mas)	ϕ (deg)	i (deg)
2.2	3.75 ± 0.16	4.93 ± 0.062	76.8 ± 3.0	$112. \pm 1.7$	45.0 ± 1.2
7.7	0.894 ± 0.13	10.3 ± 0.87	$99.3 \pm 15.$	$120. \pm 13.$	45.3 ± 8.8
8.7	0.398 ± 0.024	11.3 ± 0.56	96.5 ± 6.6	$114. \pm 8.1$	43.7 ± 5.5
9.7	0.176 ± 0.012	12.8 ± 1.1	$113. \pm 7.8$	$131. \pm 13.$	43.1 ± 7.4
11.7	0.191 ± 0.013	14.6 ± 1.1	$114. \pm 5.9$	$130. \pm 11.$	42.2 ± 6.6
12.4	0.190 ± 0.014	15.3 ± 1.2	$121. \pm 6.4$	$134. \pm 14.$	42.1 ± 7.0

ties in the best-fit values were derived using the same Monte-Carlo approach described by Boley et al. (2013).

We tabulate the results of this fitting procedure for each wavelength in Table 2, and show the observed and model visibilities in Fig. 5. The visibilities are plotted in terms of the deprojected spatial frequency \mathcal{R} ,

$$\mathcal{R} = \sqrt{u_\phi^2 + v_\phi^2 \cos^2 i}, \quad (1)$$

where

$$u_\phi = u \cos \phi - v \sin \phi \quad (2)$$

$$v_\phi = u \sin \phi + v \cos \phi \quad (3)$$

and u and v are the spatial coordinates of the interferometric observations. The inclination angle i and position angle ϕ are taken from the best-fit values for each wavelength in Table 2.

We find that the two-dimensional parameters derived from the 2.2 μm data are essentially identical to those derived by

Kraus et al. (2010) for the same data set. However, in contrast to the present work, the relative flux and size of the one-dimensional Gaussian component in their model were not free parameters: we find a FWHM size of 77 mas (compared to their fixed value of 108 mas), and a relative flux of the one-dimensional Gaussian of 27% (compared to their fixed value of 15%).

The orientation derived from the mid-infrared data matches that derived from the near-infrared observations to within ~ 10 – 20° , which Kraus et al. (2010) showed to be perpendicular to the large-scale outflow, and interpreted as originating from a circum-stellar disk. Thus, for this particular MYSO, the mid-infrared emission of the compact component is clearly aligned with the expected orientation of the disk². Furthermore, the widths of the two-dimensional Gaussians in the fit increase with wavelength. Similar behavior was also seen by Kraus et al. (2010) in the spectrally-resolved near-infrared data, and is indicative of a

² N.B., this is not always the case. See the discussion of individual sources in the VLTI/MIDI MYSO Survey (Boley et al. 2013).

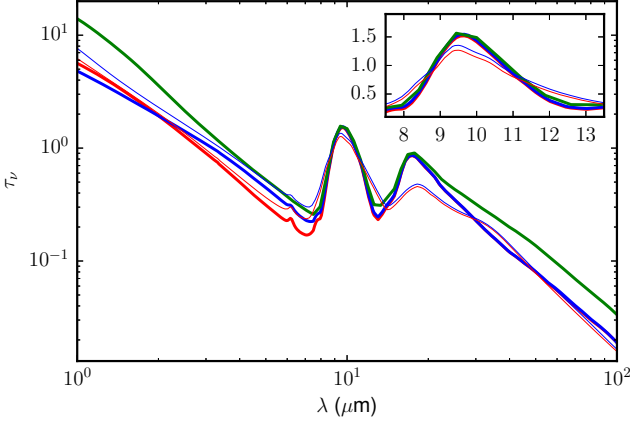


Fig. 4. Derived optical depth of the foreground extinction, for different types of carbonaceous grains and size distributions. The thick red and blue curves utilize the Milky-Way size distributions from Weingartner & Draine (2001) for the $R_V = 3.1$ and $R_V = 5.5$ extinction laws, respectively, using PAH and graphite grains. The thick green curve utilizes the MRN size distribution with graphite grains. All three curves include the silicate contribution derived by Boley et al. (2013). For comparison, the synthetic extinction curves of Weingartner & Draine (2001), which differ in their silicate content, are shown as thin red ($R_V = 3.1$) and blue ($R_V = 5.5$) curves.

temperature gradient: i.e., the source looks larger at longer wavelengths (lower temperatures). We thus confirm that the temperature gradient detected by Kraus et al. (2010) is also apparent at N -band wavelengths.

4.2.2. Temperature-gradient disk models

The Gaussian fits presented in Section 4.2.1 provide a simple way to examine the general source morphology at different wavelengths. However, such Gaussian fits are an ad-hoc solution to the problem of fitting visibilities, rather than a physically-motivated model with meaningful physical parameters.

An attractive alternative to the Gaussian models is a model consisting of a geometrically-thin, optically-thick (i.e., emitting as a black body) disk with a temperature distribution parameterized by a power law, i.e.

$$T(r) = T_{\text{in}} \left(\frac{r_{\text{in}}}{r} \right)^p \quad r_{\text{in}} < r \leq r_{\text{out}}, \quad (4)$$

where T_{in} is the temperature at the inner radius r_{in} of the disk. Such a temperature gradient follows from several theoretical studies of disk structure (for an overview, see the textbook by Hartmann 2009, and references therein), and has been applied to T Tauri stars (Eisner et al. 2005; Vural et al. 2012), Herbig stars (Eisner et al. 2007; Benisty et al. 2011; Ragland et al. 2012; Chen et al. 2012; Kraus et al. 2013; Vural et al. 2014b,a), MYSOs (Kraus et al. 2010; Boley et al. 2012) and other objects (e.g. Malbet et al. 2005; Kreplin et al. 2012; Kraus et al. 2012; Wang et al. 2012).

This model provides a single physical structure which can emit at a variety of wavelengths and scales. For additional information on constructing the visibility function for such a disk, we refer to the work by Eisner et al. (2007). As in Section 4.2.1, we also include an extended component in the form of a one-dimensional Gaussian “halo.” However, as this extended component is not well probed by our data, we do not attempt to ascribe a predefined wavelength dependence to the halo parameters. Thus,

Table 3. Fit parameters for temperature-gradient disk models

Parameter	Model 1	Model 2
T_{in} (K)	1500 [†]	1760
r_{in} (mas)	1.55	1.78
p	0.616	0.840
ϕ_{disk} (deg)	112	107
i_{disk} (deg)	42.3	47.6
$F_{\text{disk}}/F_{\text{halo}}$		
$\lambda = 2.2 \mu\text{m}$	3.45	3.10
$\lambda = 7.7 \mu\text{m}$	1.61	0.750
$\lambda = 8.7 \mu\text{m}$	0.644	0.370
$\lambda = 9.7 \mu\text{m}$	0.279	0.250
$\lambda = 11.7 \mu\text{m}$	0.347	0.246
$\lambda = 12.4 \mu\text{m}$	0.369	0.246
$\text{FWHM}_{\text{halo}}$ (mas)		
$\lambda = 2.2 \mu\text{m}$	76.8	69.9
$\lambda = 7.7 \mu\text{m}$	142	61.2
$\lambda = 8.7 \mu\text{m}$	120	84.1
$\lambda = 9.7 \mu\text{m}$	132	117
$\lambda = 11.7 \mu\text{m}$	126	106
$\lambda = 12.4 \mu\text{m}$	138	107
χ_r^2	0.613	2.98

Notes. [†] Kept fixed during the fitting procedure.

Model 1 was fit to the visibilities only (Section 4.2.2); Model 2 was fit to a combination of the visibilities and correlated fluxes (Section 4.3.1).

the relative flux and size of the halo are fit independently for all wavelengths, while the disk parameters are fit simultaneously for all wavelengths.

The results of fitting this model for a *fixed* inner temperature of the disk of $T_{\text{in}} = 1500$ K (approximating the evaporation temperature of silicate grains) to the K - and N -band visibility amplitudes are shown in Fig. 6 and in Table 3 (Model 1).

The quality of the fit is good ($\chi_r^2 = 0.613$). The disk position angle and inclination angle derived are similar to those found for the Gaussian models, and perpendicular to the large-scale outflow shown by Kraus et al. (2010) and Caratti o Garatti et al. (2015). However, the inner temperature of the disk cannot be determined by fitting the visibilities alone. For example, if we allow T_{in} to be a free parameter when fitting only the visibilities, we do find a formally “better” fit (not shown; $\chi_r^2 = 0.538$); but with an inner disk temperature of $T_{\text{in}} = 7490$ K at a radius of $R_{\text{in}} = 1.02$ mas (3.6 AU at a distance of 3.6 kpc), and a total integrated power output of $\sim 5 \times 10^6 L_{\odot}$, such a model is clearly unphysical, underlying our conclusion that fitting *only* the visibilities or *only* the SED with (semi-)physical models can lead to nonsensical results (for comparison, the total luminosity for this source derived by the RMS survey (Urquhart et al. 2007) is lower by a factor of $\sim 10^2$).

4.3. Model fits to the visibilities and correlated fluxes

The model fits to the visibilities presented in the previous section are useful for gauging the appearance of IRAS 13481-6124 at different wavelengths. However, as mentioned in the previous section, fitting the visibilities alone does not restrict the models (specifically, by the temperature-gradient disk models) to be consistent with the SED. As a next step, we embark on extracting some basic physical parameters by means of comparing both the spatial *and* spectral data to more elaborate models.

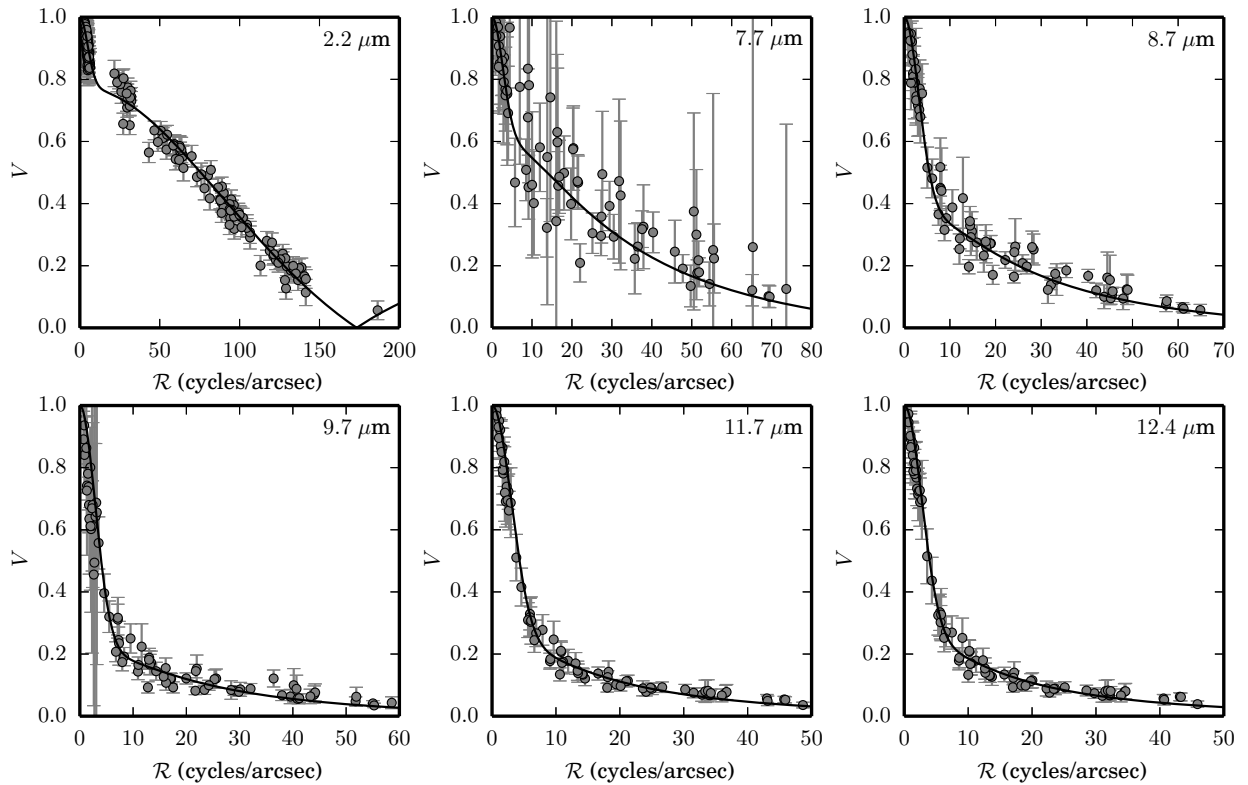


Fig. 6. Temperature-gradient disk model fits to the visibilities for a disk with $T_{\text{in}} = 1500$ K (fixed; Model 1), plotted as a function of deprojected spatial frequency. See Table 3 (Model 1) for the fit parameters. Circles and error bars mark the observations, while the model fits to each wavelength are shown as a solid curve.

Several previous studies of lower-mass, less-embedded stars utilize similar models to successfully reproduce both the visibilities and the entire SED (e.g. Malbet et al. 2005; Eisner et al. 2007; Ragland et al. 2012; Vural et al. 2012; Wang et al. 2012). However, this technique is not directly applicable to deeply-embedded objects, as the SED is dominated by the circumstellar envelope (rather than the central star and disk) at all wavelengths. At optical and near-infrared wavelengths, and in the N -band within the silicate feature, the emission from the star and/or disk is heavily absorbed and reddened by the envelope. At far-infrared/sub-millimeter wavelengths, the emission from the envelope itself, which typically contains the vast majority of the mass of the system, dominates the SED.

In principle, the extinction caused by the envelope can be accounted for at near- and mid-infrared wavelengths by reddening the model flux values (or, equivalently, by dereddening the observed fluxes). However, as mentioned in Section 4.1, this cannot be done reliably at near-infrared wavelengths (see also the detailed discussion in Section 5.3). On the other hand, the optical depth derived in the N -band, which is dominated by the silicate feature, is essentially independent of the type of carbonaceous grains or the size distribution used, suggesting the determination of the (total) extinction at these wavelengths to be relatively robust.

We therefore use the following approach for the model fitting in this section. We fit the dereddened N -band correlated flux measurements (the measured correlated fluxes were dereddened using the $R_V = 5.5$ extinction law derived in Section 4.1), and, at the same time, the K -band visibilities (which are unaffected by extinction). This hybrid approach of using correlated flux lev-

els and visibilities together allows us to make the best usage of the information available in the observations, without over-interpreting the near-infrared flux measurements by imposing a highly-uncertain near-infrared extinction correction. As in Section 4.2.2, both the spatial information and wavelength coverage are still represented in the fitting process, but now the energy budget is also constrained by the mid-infrared measurements.

4.3.1. Temperature-gradient disk models

Applying this combined approach to the temperature-gradient disk model presented in Section 4.2.2 allows us to leave the inner temperature of the disk T_{in} as a free parameter. We present the results of the fitting procedure in Table 3 (Model 2), Fig. 7 (interferometric data) and Fig. 8 (total N -band spectrum).

Given the simplicity of this model and the wide range of wavelengths and baselines fit, we regard this fit as good, despite having a larger χ_r^2 value of 2.98. In particular, we note that the N -band correlated fluxes at long baselines, where the disk emission dominates, are well reproduced by this model, despite the assumption that the disk emits as a black body (i.e. it is not necessary to include a silicate emission feature to reproduce the observed correlated flux levels). As with Model 1, the derived position angle and inclination angle of the disk are perpendicular to the large-scale outflow. We derive a temperature of 1760 K for the inner disk, which is fully consistent with the expectation that the inner radius is set by the dust evaporation temperature. As in the case of Model 1, the majority of the *total* mid-infrared flux originates from the halo, suggesting a circum-

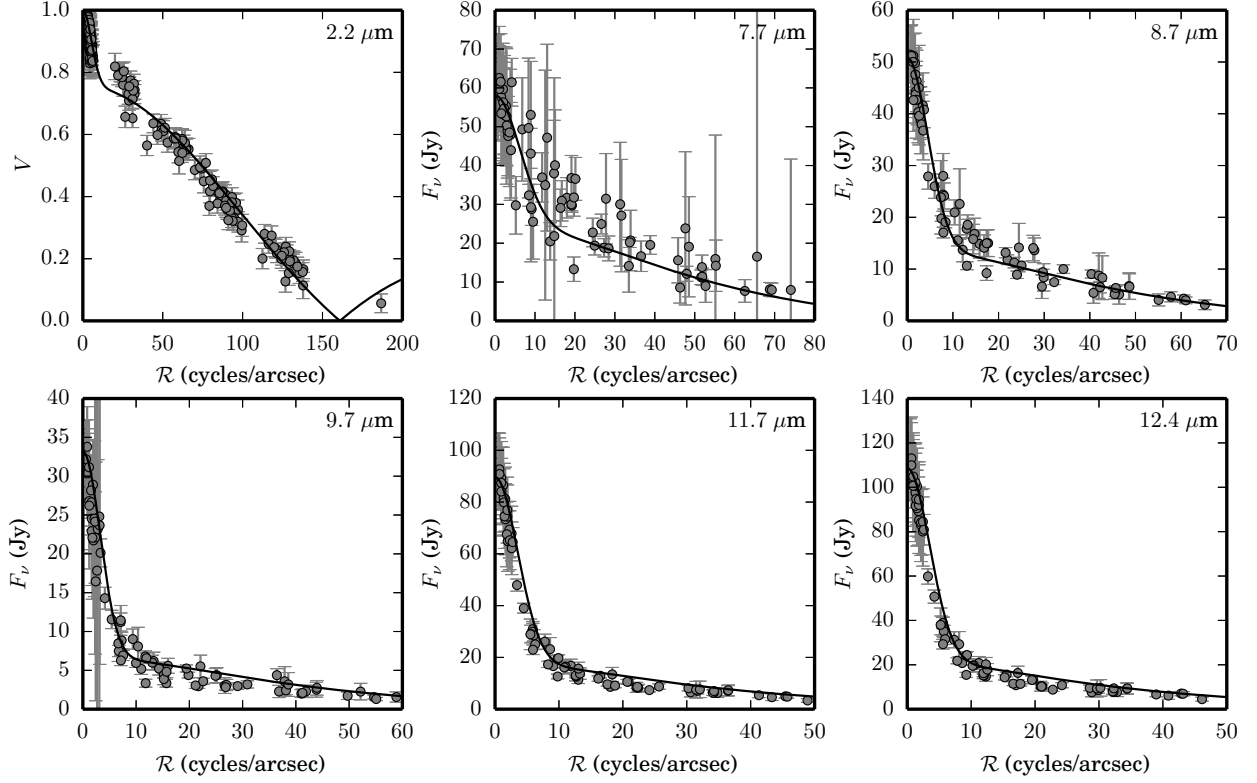


Fig. 7. Temperature-gradient disk model fits to the *K*-band visibilities and *N*-band correlated fluxes (with T_{in} treated as a free parameter), plotted as a function of deprojected spatial frequency. See Table 3 (Model 2) for the fit parameters. Circles and error bars mark the observations, while the model fits to each wavelength are shown as a solid curve.

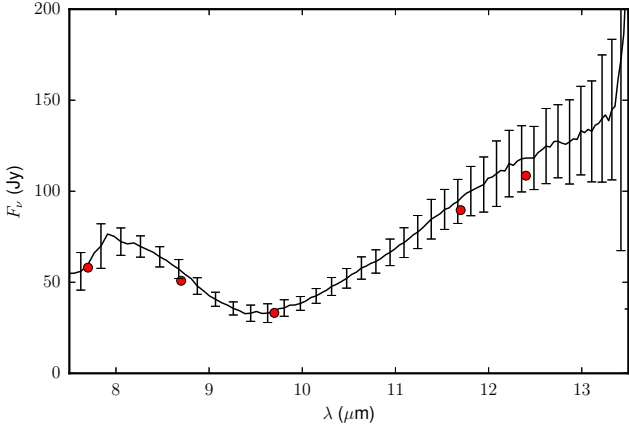


Fig. 8. Total *N*-band flux levels for the model fit to the *K*-band visibilities and *N*-band correlated fluxes. The flux levels predicted by the model are shown as red points. The black curve and error bars show the MIDI spectrum, observed with the **prism**.

stellar disk makes only a relatively small contribution to the total mid-infrared emission.

4.3.2. Radiative transfer models

Kraus et al. (2010) presented a radiative-transfer model of IRAS 13481-6124 based on available SED information and *K*-band interferometric observations. We note, however, that the modeling efforts presented in that work do not reproduce the ini-

tial drop seen in the visibility amplitude in the *N*-band at low spatial frequencies (see Fig. B.1). As noted in Sec. 4.2, the interferometric observations in the *N*-band show the presence of two emission components, with the larger component (i.e., the “halo”) contributing most of the total flux. This halo is also clearly manifest in the *K*-band visibilities as a steep initial drop (e.g. Fig. 5), which arises from scattered light from the envelope.

In this section we explore the nature of these two separate emission components, making use of radiative-transfer calculations. For this exercise, we use the radiative-transfer code developed by Whitney et al. (2003b,a), which is the same code used by Kraus et al. (2010) to model the *K*-band interferometric observations of this object. The radiative transfer code produces images and spectra, which we convert into visibilities and correlated fluxes. We use this code for consistency with that work, and also because it allows the inclusion of an envelope, with cavities carved out by a polar outflow. Heated cavity walls have been claimed to be responsible for the *N*-band emission at scales of ~ 100 AU in other MYSOs (e.g. de Wit et al. 2010, 2011), and this could be a natural explanation for the two-component nature of the emission.

As in Sec. 4.3.1, we limit ourselves to modeling the *K*-band visibilities and the *N*-band correlated fluxes. We do not attempt to reproduce the entire SED with these models. We explore three classes of models, consisting of a disk only, an envelope (with a 10° cavity) only, and a disk plus an envelope (also with a 10° cavity). The disk structure is parameterized by a standard accretion disk, with a scale height given by $H(r) = H_0(r_{\text{in}}/r)^\beta$ ($\beta = 1.0$), and a vertically-truncated inner rim. The surface density distribution of the disk is adopted to be a power law with an

Table 4. Parameters of radiative-transfer models

Model	\dot{M}_{env} ($M_{\odot} \text{ yr}^{-1}$)	M_{disk} (M_{\odot})	r_{in} (AU)	ρ_{cav} (g cm^{-3})	ρ_{amb} (g cm^{-3})
Disk only	—	20	9.7	—	—
Envelope only	4×10^{-4}	—	—	7.7×10^{-20}	9.1×10^{-21}
Disk and envelope	2.65×10^{-4}	2.5×10^{-3}	6.4	7.7×10^{-20}	9.1×10^{-21}

index of -1.0 . We fix the outer radius of the disk to 1000 AU (e.g. de Wit et al. 2009), and adjust both the inner radius r_{i} and mass M_{disk} in our fits. The envelope structure is described by Eq. (1) from Whitney et al. (2003b), and is parameterized by the mass-infall rate of the envelope \dot{M}_{env} , which we adjust as a fitting parameter, and the centrifugal radius R_{c} , which we also fix to 1000 AU. The outer radius of the envelope was adopted to be 50 000 AU. The values of \dot{M}_{env} quoted here merely parameterize the density structure of the envelope, and do not represent a true mass-infall rate. We use the same dust for the disk and envelope components (MRN-60SiI). The dust opacity is set to zero in regions where the dust temperature is found to be in excess of 1600 K. Because it is not known in detail how the disk structure will change in the presence of an infalling envelope, we adopt these geometrically-simple structures. For the central source, we adopt an O8V star with $T_{\text{eff}} = 33400$ K and $R_{\star} = 8.5 R_{\odot}$ (Martins et al. 2005). The results of the three classes of radiative-transfer models are shown in Fig. 9 and summarized in Table 4.

In the disk-only model (red lines in Fig. 9), we have adopted the disk mass from Kraus et al. (2010). In that work, they calculated the formal dust sublimation radius to be between 6.2 and 10.9 AU, for an adopted luminosity of $34\,600 L_{\odot}$ (at a distance of 3.2 kpc). Scaling this to our adopted values by the square root of the luminosity, we obtain a dust sublimation radius between 9 and 16 AU (or between 2.6 and 4.5 mas at a distance of 3.6 kpc). For a geometric ring model, the K -band visibilities indicate $\theta = 5.4$ mas (Kraus et al. 2010), which translates to an inner disk radius of 9.7 AU, and which we adopt as the inner radius for the disk-only model³. A circumstellar disk alone can only account for the observed flux spectrum if additional dust extinction ($A_V = 50$ mag) is imposed, which provides an ad-hoc approximation for the absorption due to the envelope. The disk emission can be made to fit the high-spatial-frequency tail in the N -band correlated fluxes, however the correlated flux predicted at low spatial frequencies is significantly lower than the observed values. Furthermore, the initial drop seen in the observed K -band visibilities is also not present. In other words, the disk-only model cannot reproduce the larger-scale emission seen in the object. We experimented with the hydrostatic equilibrium solution in order to increase the index β (and, correspondingly, the disk flaring angle) in order to make the disk brighter on larger (≥ 50 AU) spatial scales, however, this did not improve the fit. We underline that, according to standard disk theory and hydrostatic equilibrium, the index of the surface-density power law should lie between -1.0 and -1.5 (e.g. D’Alessio et al. 1998; Armitage 2010).

We also explored the possibility of whether or not the interferometric observations could be reproduced using a model consisting only of an envelope with a cavity, without any contribution from a disk and without additional foreground absorption

applied. This was the approach used in previous studies of some MYSOs (e.g. de Wit et al. 2010). For this envelope-only model (green lines in Fig. 9), we find that we can reproduce the emission at low spatial frequencies, but the correlated flux levels at high spatial frequencies are far too low. The K -band visibilities are also significantly lower than those observed. In other words, contrary to the disk-only model, the extended emission is reproduced well, but there is far too little emission at scales of a few tens of AU. Clearly, one can anticipate that a combination of an envelope and a disk will be able to reproduce the observed correlated flux levels at both scales.

The combined disk and envelope model is shown in blue in Fig. 9. Here, we have decreased the mass of the disk from $20 M_{\odot}$ to just $2.5 \times 10^{-3} M_{\odot}$, which has negligible effect on the visibility and correlated flux levels, as the disk is optically thick at infrared wavelengths in both cases. The inner radius of the disk was decreased to 6.4 AU, i.e. the inner radius of our best fit to the K -band visibilities and the N -band correlated fluxes using the temperature gradient disk (Model 2 in Table 3; see Sec. 4.3.1). Although the final model produces an acceptable fit over all size scales and nearly the full N band, it is clear that at the short wavelength edge ($7.7 \mu\text{m}$) the combined disk and envelope model produces fluxes lower than those observed. Nonetheless, comparing the model visibilities to those obtained in the K band, we find a reasonable correspondence for the combined disk and envelope model. Although the spread in visibilities between position angles parallel and perpendicular to the disk is larger than observed, the initial drop in visibilities due to the envelope compares well, which implies that some of the asymmetries seen in the K -band disk image (related to the disk rim) are in reality much smaller than in the dust-only radiative-transfer models.

5. Discussion

5.1. Summary of modeling results and the structure of circumstellar material around IRAS 13481-6124

In this work, we have used a variety of progressively-complicated approaches to model the interferometric observations of IRAS 13481-6124, all of which attempt to unravel the distribution of the circumstellar dust surrounding the object.

The Gaussian fits to the visibility (Sec. 4.2.1) at each wavelength all indicate the presence of a compact ($5 - 15$ mas) component, elongated approximately along the expected direction of the disk (i.e., perpendicular to the large-scale outflow reported by Kraus et al. (2010)). Besides the compact component, these models also include a more extended “halo” component, which spans $75 - 120$ mas, depending on wavelength. The relative flux of this halo component grows with wavelength, containing only 21% of the total flux at $2.2 \mu\text{m}$, and a full 84% of the total flux at $12.4 \mu\text{m}$ (see Table 2).

Kraus et al. (2010) interpreted the compact, K -band emission as arising from a circumstellar disk. This position is supported by both geometrical arguments (the elongated structure

³ We note that this value is significantly larger than the inner radius found for the temperature-gradient disk models (see Table 3).

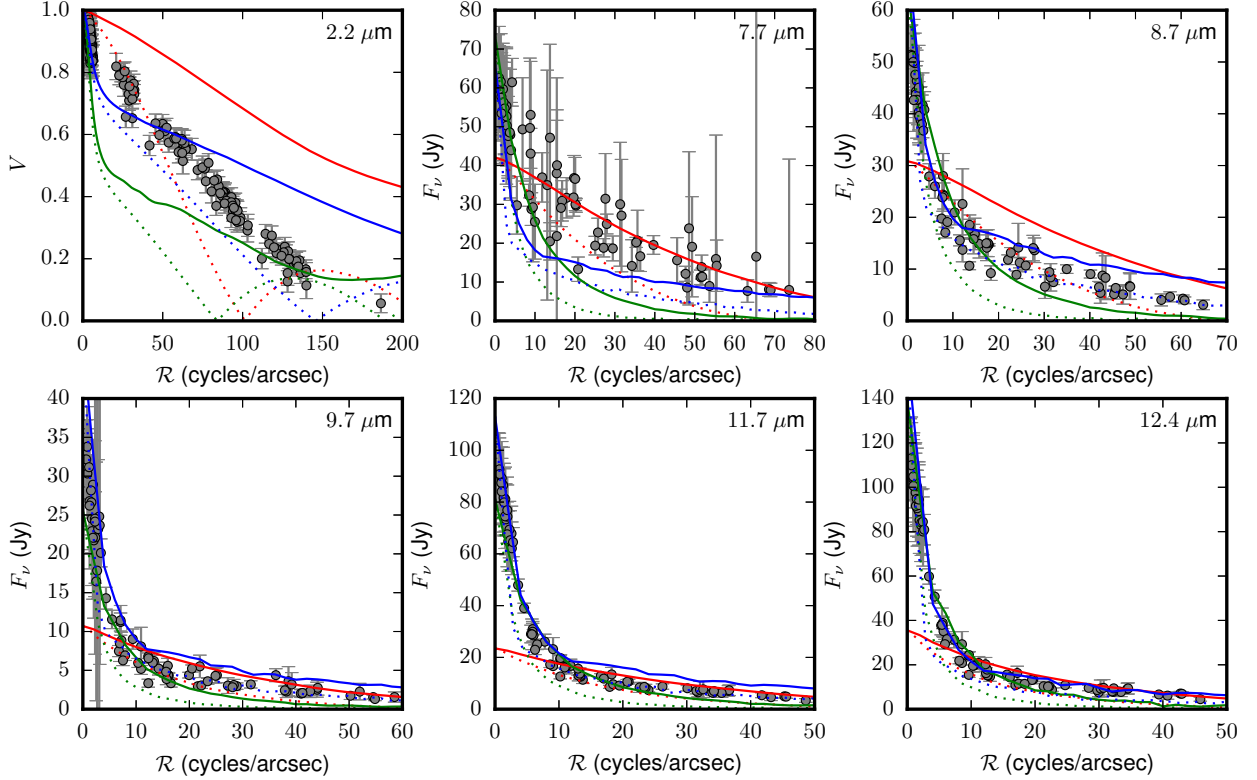


Fig. 9. Visibility/correlated flux levels predicted by radiative-transfer models, plotted as a function of deprojected spatial frequency. The observations are shown in gray. The disk-only model is shown in red, the envelope-only model is shown in green, and the combined disk and envelope model is shown in blue, where the solid and dotted lines show the visibility perpendicular and parallel to the disk, respectively. See Table 4 for the fit parameters.

seen is oriented perpendicular to a large-scale outflow) and the radiative-transfer model presented in that work. Both the orientation and the axial ratio (given by $1/\cos i$) of the compact component seen in the N band are similar to those of K band. Thus, it is tempting to also attribute this emission to a circumstellar disk. However, both numerical calculations by Zhang et al. (2013) and Q -band ($\lambda = 20 \mu\text{m}$) observations of MYSOs by Wheelwright et al. (2012) indicate that outflow cavities probably play a more significant role at mid-infrared wavelengths. Therefore, caution is warranted in interpreting our N -band interferometric observations.

The geometric fits to the visibilities and correlated fluxes with the temperature-gradient disk model, presented in Sec. 4.2.2 and 4.3.1, support the hypothesis that the *compact* emission seen at both wavelength ranges can be explained by a single physical structure, in this case a geometrically-thin, optically-thick circumstellar disk. By fitting the (dereddened) N -band correlated flux levels (Sec. 4.3.1) with this simple model, we are able to derive a value of 1760 K for the inner temperature of the disk, consistent with expectations for a dusty disk.

The radiative transfer models employed in Sec. 4.3.2, which we use to explore the effects of the outflow cavity on the interferometric observations, also indicate that long-baseline correlated fluxes arise specifically due to the disk (and not due to the outflow cavity). Furthermore, by allowing us to experiment with different disk geometries (unlike the temperature-gradient disk), the radiative transfer models show that the short-baseline measurements *can not* be reproduced by a disk alone, even by increasing the flaring angle of the disk.

By including an envelope in the radiative transfer models, we are able to reproduce the observed N -band correlated flux levels at short baselines, as well as the initial drop seen in the K -band visibilities. These models also indicate that the vast majority of the total flux at mid-infrared wavelengths arises due to the inner edges of the envelope, rather than from the disk. However, despite this fact, a disk extending inwards to ~ 6 AU is still required in order to reproduce the long-baseline correlated flux levels at mid-infrared wavelengths, as well as the relatively high K -band visibilities.

We explored the effects of the cavity density (ρ_c) and the ambient density (ρ_{amb}) (the minimum density threshold) on the radiative-transfer model fits. For both cases with an envelope, we adopted values of $\rho_c = 7.7 \times 10^{-20} \text{ g cm}^{-3}$ and $\rho_{\text{amb}} = 9.1 \times 10^{-21} \text{ g cm}^{-3}$. At low spatial frequencies, we found that the cavity density itself does not matter, as long as it is substantially less than that of the envelope and disk. For high spatial frequencies, increasing the cavity density slightly decreases the correlated flux due to increased absorption at these scales. The ambient density was found to be degenerate with both the mass infall rate and the envelope size, i.e. it is possible to construct many models with the same total extinction by varying these parameters.

Among the proposed models for outflow creation, the wide-angle wind (Li & Shu 1996) and the jet bow-shock model (Chernin & Masson 1995) explain the observed outflow properties best (Lee et al. 2000, 2001; Frank et al. 2014). Lee et al. (2001) showed that, for simulations of isothermal winds, a post-shock number density of $10^3 - 10^4$ is seen. For bow-shock mod-

els, number densities of 10^4 are produced in the post-shock region. The densities varies between the low- and high-velocity parts of the outflow; however, for the scales the interferometer is sensitive to ($\sim 10 - 100$ AU), we assume that the cavity density changes very little, and, based on previous work, we adopt a value of $n = 10^4 \text{ cm}^{-3}$ ($2.3 \times 10^{20} \text{ g cm}^{-3}$).

As pointed out by Kraus et al. (2010), the disk mass is not constrained by the interferometric data. Their estimate of the disk mass ($20 M_{\odot}$) was performed by varying the disk mass of the adopted envelope description and observing the subsequent effects on the model SED. Given that most of the disk mass is at cold temperatures, and that the disk is optically thick at infrared wavelengths, (sub)mm observations are required to make a more accurate estimate of the disk mass. Indeed, we find that radiative-transfer models with a disk mass of $20 M_{\odot}$ or $10^{-2} M_{\odot}$ do not produce a significant difference in the infrared correlated fluxes and visibilities. The calculated disk surface temperatures are similar in both cases (within the first 100 AU), apart from the different hydrostatic equilibrium solution, which produces a higher sublimation for the more massive (denser) disk. A disk more massive than $20 M_{\odot}$ produces higher temperatures farther out ($\gtrsim 100$ AU) at the disk surface, increasing the total flux, but not the correlated flux MIDI is sensitive to.

Although Kraus et al. (2010) used SED modeling to attempt to constrain the disk mass, due to the inherent uncertainties in modeling the SEDs of MYSOs (see Sec. 4.1, and a more detailed discussion in Sec. 5.3), we believe there is currently no way to reliably (even approximately) determine the mass of the disk around IRAS 13481-6124 using existing observational data. High-angular-resolution ALMA observations will be able to estimate the disk mass from the optically thin (sub)-millimeter continuum emission, although it would still be necessary to discriminate between the disk and envelope contributions. The most promising approach, in our opinion, would be to use spatially-resolved observations of gas lines with ALMA in order to construct a kinematic model of the disk, and determine the enclosed mass (including the stellar mass) as a function of radius (e.g. Johnston et al. 2015). Until this is done, for this object and other similar MYSOs, the question of the disk masses around such objects remains an open question.

5.2. Prospects for future observations

Infrared interferometry, be it in the near- or mid-infrared, is one of only a few ways to observe systems like IRAS 13481-6124 with the required spatial resolution ($\lesssim 10$ mas) to resolve the inner regions of the dust disk. While the three-telescope beam combiner of AMBER was able to provide sufficient uv coverage to allow Kraus et al. (2010) to reconstruct an image from the near-infrared interferometric observations, achieving adequate uv coverage with a two-telescope instrument like MIDI (now decommissioned) is essentially impossible. This is due to the large amount of observational time required to observe a sufficient number of projected baselines, as well as the inherent limits on the information which can be recovered from the interferometric phase using a two-telescope instrument (Monnier 2007).

The MATISSE instrument (Lopez et al. 2008), which will be one of the second-generation interferometric facilities at the VLTI, is expected to come online in the near future. This new instrument will not only simultaneously utilize four telescopes (either the 1.8-m ATs or the 8.2-m UTs), but also open up the L ($3 - 4 \mu\text{m}$) and M ($4 - 6 \mu\text{m}$) bands for interferometric observations, in addition to providing full, simultaneous coverage of the N band. As a result, a single observation with MATISSE

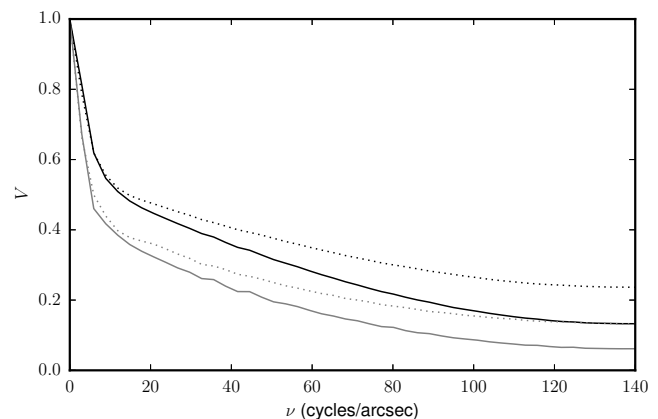


Fig. 10. Predicted visibility levels in the L (black) and M (gray) bands. The solid and dotted lines show the visibility perpendicular and parallel to the disk, respectively.

will provide spectrally-resolved visibility amplitudes for six projected baselines, as well as four determinations of the closure phase, simultaneously in two wavelength bands (either $L+N$ or $M+N$). Using MATISSE, it will therefore be feasible to create a model-independent image reconstruction of the source at a variety of mid-infrared wavelengths, much as Kraus et al. (2010) did in the K band using AMBER, rather than being limited to the simple geometric models presented in this paper.

In anticipation of these new observational possibilities, we use the combined disk and envelope radiative-transfer model from Sec. 4.3.2 to predict the visibility levels in the L and M bands, which we show in Fig. 10. We see that the behavior of the visibility in both wavelength ranges can be split into three spatial frequency ranges. For low spatial frequencies ($\lesssim 10$ cycles/arcsec, $V \gtrsim 0.5$), we see that the envelope still dominates, containing half of the total flux. For spatial frequencies in the range of $\sim 20 - 120$ cycles/arcsec ($0.2 \lesssim V \lesssim 0.5$), the disk becomes evident, with a significant variation in the visibility level for position angles perpendicular and parallel to the disk. Finally, at high spatial frequencies ($\gtrsim 120$) cycles/arcsec, the visibility flattens off due to the unresolved central source.

In terms of projected baselines, the disk will be optimally resolved for baselines of $7 - 90$ m in the L band, and baselines of $10 - 120$ m in the M band. This puts the disk just beyond the diffraction limit of single 10-m class telescopes, but perfectly in the range of projected baselines available at the VLTI (currently up to ~ 128 m). Given that the source is also very bright at these wavelengths (3.0 mag in the $3.4 \mu\text{m}$ W1 filter and 1.3 mag in the $4.6 \mu\text{m}$ W2 filter of WISE; Cutri et al. 2012) IRAS 13481-6124 therefore represents an ideal target for MATISSE.

5.3. On radiative-transfer modeling of deeply-embedded sources

At near-infrared wavelengths, where much of the emission from the circumstellar disk is expected to originate, extinction from the circumstellar envelope is already significant. As discussed in Section 4.1, the amount of extinction is strongly dependent on the type of carbonaceous grains and size distribution adopted. Due to the lack of spectral features at infrared wavelengths, which might otherwise be used to constrain the composition and size distribution of carbonaceous grains, it is impossible to reliably predict the amount of extinction caused by the envelope,

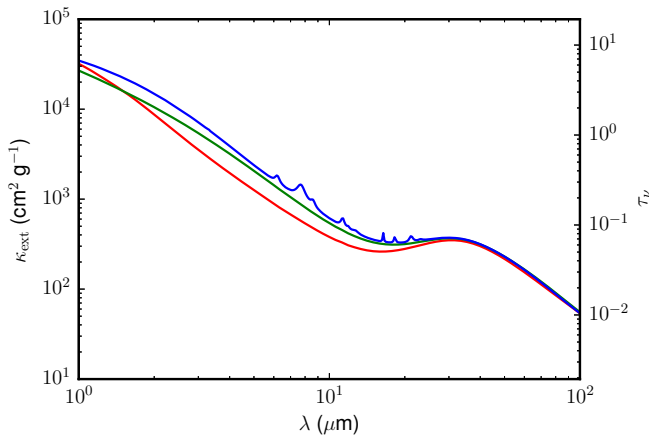


Fig. 11. Near- and mid-infrared extinction derived for carbonaceous grains, using the size distributions of Mathis et al. (1977), shown in red; Kim et al. (1994), shown in green; and Weingartner & Draine (2001), shown in blue. The vertical axis shows the mass extinction coefficient on the left and the optical depth on the right, where a value of $3.8 \times 10^{-4} \text{ g cm}^{-2}$ has been used for the column density of the carbonaceous material (see Section 5.3).

and therefore the amount of emission from the circumstellar disk, at wavelengths $\lesssim 8 \mu\text{m}$.

We illustrate this point in Fig. 11, where we show the infrared extinction properties obtained for carbonaceous dust for three commonly-used grain size distributions: the classical MRN power-law distribution (Mathis et al. 1977); the parameterized distribution of Kim et al. (1994, hereafter “KMH”), which is a power law with exponential decay for large grains; and the more elaborate “Milky Way” size distribution of Weingartner & Draine (2001, hereafter “WD”). In all three cases, we have used the graphite grain properties from Laor & Draine (1993); for the WD size distribution, we also use the PAH grains of Li & Draine (2001) for the small grains, following the prescription given by Weingartner & Draine (2001)⁴. We show the mass extinction coefficient κ_{ext} , and also the extinction optical depth τ_v , where we have adopted a column density of the carbonaceous material of $3.8 \times 10^{-4} \text{ g cm}^{-2}$. This value was chosen based on the estimate of $5.7 \times 10^{-4} \text{ g cm}^{-2}$ for the silicate column density by Boley et al. (2013), assuming a standard mass ratio of 60:40 for silicates and graphite (Dwek et al. 1997).

The three extinction curves in Fig. 11 represent three reasonable, equally fair (given the information available) “best guesses” for the contribution of carbonaceous grains to the dust composition of the envelope. However, the choice between these three (or any other) size distributions/extinction curves will *strongly* influence the extinction at short wavelengths. For example, in the *K* band ($\lambda = 2.2 \mu\text{m}$), the optical depths $\tau_v(2.2 \mu\text{m})$ for the extinction curves constructed using the MRN, KMH and WD size distributions are 2.7, 3.5 and 4.8, respectively. Consequently, the reddened *K*-band flux values (which scale as $e^{-\tau_v(\lambda)}$) will be smaller by factors of 15 (MRN), 32 (KMH) and 130 (WD). In other words, for deeply-embedded sources, even the *order of magnitude* of the amount of attenuation from the envelope at near-infrared wavelengths is difficult to determine.

⁴ At these wavelengths, the presence or absence of PAH grains does not affect the continuum opacities, and the only effect of the PAH grains on the derived extinction are the mid-infrared PAH bands. Therefore, PAHs cannot be used to restrict the infrared continuum extinction.

Clearly, this is a very large uncertainty when attempting to (simultaneously) model the emission from hot dust at these wavelengths⁵.

6. Summary and conclusions

In this work, we have presented new *N*-band interferometric observations of the massive young stellar object IRAS 13481-6124, obtained using aperture masking with T-ReCS on Gemini South, and long-baseline measurements with MIDI on the VLTI. We have examined the extinction in the wavelength range of $\sim 1 - 13 \mu\text{m}$ for this source, and performed a comprehensive analysis of interferometric observations of the object in both the *K* and *N* band, using both geometric and radiative-transfer models.

On the basis of the geometric models, we have shown that both the *K*-band visibilities and the *N*-band correlated fluxes can, simultaneously, be well fit by a system consisting of a geometrically-thin, optically-thick circumstellar disk, and an extended halo. In the *K* band, the disk is the dominant source of emission, producing $\sim 76\%$ of the total flux. In the *N* band, however, the situation is reversed, with the disk contributing only $\sim 20 - 43\%$ of the total flux, depending on wavelength. For our preferred model, the disk is inclined at $\sim 48^\circ$, and the position angle of the semi-major axis is 107° . We find the inner radius of the disk to be at $\sim 1.8 \text{ mas}$, with a temperature of 1760 K. The temperature gradient of the disk is well described by a power law with an index of -0.84 .

Using radiative transfer models, we have confirmed that a circumstellar disk, by itself, is unable to produce the high visibilities/large correlated-flux values observed in the *N* band at short baselines. Furthermore, we found that the extended emission in the *N* band (i.e., the “halo” in the geometric models) can be well reproduced by an outflow cavity, implying that the vast majority of the *N*-band emission arises from the outflow cavity, rather than the disk. We have also shown that the infrared emission from the disk is optically thick, and that the disk emission can be equally well explained with disk masses ranging from $\sim 10^{-3}$ to $\sim 10^1 M_\odot$.

By comparing various extinction laws and considering their applicability to this deeply-embedded object, we have shown that the near-infrared absolute flux levels are completely unconstrained. This is due to the uncertain carbonaceous content of the envelope, which dominates the extinction law at $\lambda \lesssim 8 \mu\text{m}$. The near-infrared SED therefore contains very little (if any) information about the disk. In light of this, since previous determinations of the disk mass have relied on modeling the SED, we argue that the disk mass of IRAS 13481-6124, and, indeed, for other similar deeply-embedded massive young stellar objects, cannot be determined without spatially-resolved observations in the (sub-)millimeter continuum and/or the disk kinematics. On the other hand, we have shown that both the near-infrared *visibilities* and (particularly at long baselines) mid-infrared *correlated fluxes* can be used together to very effectively probe the disk geometry.

Acknowledgements. We thank the anonymous referee and editorial staff of Astronomy and Astrophysics for thoughtful critique, which led to the improvement of this manuscript. The work of PAB was supported by the Russian Science Foundation, grant No. 15-12-10017. SK acknowledges support from an STFC Ernest Rutherford fellowship (ST/J004030/1) and a Marie Skłodowska-Curie CIG grant (SH-06192). SL acknowledges support from ANR-13-JS05-

⁵ To complicate matters further, compositions, size distributions and optical properties for the *emitting* material must also be adopted, and these suffer from many of the same uncertainties already noted here.

0005 and ERC-STG-639248. JDM acknowledges support from nsf-ast1210972. We also thank Charlie Telesco, David Ciardi, Chris Packham, Tom Hayward, Adwin Boogert, Jim de Buizer and Kevin Volk for their important contributions to the Gemini/TRECS aperture masking experiment. Some observations contained herein were obtained at the Gemini Observatory (program ID GS-2007A-Q-38), which is operated by the Association of Universities for Research in Astronomy, Inc., under a cooperative agreement with the NSF on behalf of the Gemini partnership: the National Science Foundation (United States), the Science and Technology Facilities Council (United Kingdom), the National Research Council (Canada), CONICYT (Chile), the Australian Research Council (Australia), Ministério da Ciência e Tecnologia (Brazil) and Ministerio de Ciencia, Tecnología e Innovación Productiva (Argentina).

References

- Aitken, D. K., Smith, C. H., James, S. D., Roche, P. F., & Hough, J. H. 1988, *MNRAS*, 230, 629
- Armitage, P. J. 2010, *Astrophysics of Planet Formation* (Cambridge University Press)
- Beck, S. C., Fischer, J., & Smith, H. A. 1991, *ApJ*, 383, 336
- Beltrán, M. T., Brand, J., Cesaroni, R., et al. 2006, *A&A*, 447, 221
- Benisty, M., Renard, S., Natta, A., et al. 2011, *A&A*, 531, A84
- Boley, P. A., Linz, H., van Boekel, R., et al. 2012, *A&A*, 547, A88
- Boley, P. A., Linz, H., van Boekel, R., et al. 2013, *ArXiv e-prints*
- Busfield, A. L., Purcell, C. R., Hoare, M. G., et al. 2006, *MNRAS*, 366, 1096
- Caratti o Garatti, A., Stecklum, B., Linz, H., Garcia Lopez, R., & Sanna, A. 2015, *A&A*, 573, A82
- Chan, S. J., Henning, T., & Schreyer, K. 1996, *A&AS*, 115, 285
- Chen, L., Kreplin, A., Wang, Y., et al. 2012, *A&A*, 541, A104
- Chernin, L. M. & Masson, C. R. 1995, *ApJ*, 443, 181
- Churchwell, E., Babler, B. L., Meade, M. R., et al. 2009, *PASP*, 121, 213
- Cutri, R. M., Wright, E. L., Conrow, T., et al. 2012, *Explanatory Supplement to the WISE All-Sky Data Release Products*, Tech. rep.
- D’Alessio, P., Cantó, J., Calvet, N., & Lizano, S. 1998, *ApJ*, 500, 411
- de Buizer, J. & Fisher, R. 2005, in *High Resolution Infrared Spectroscopy in Astronomy*, ed. H. U. Käufel, R. Siebenmorgen, & A. Moorwood, 84–87
- de Wit, W. J., Hoare, M. G., Fujiyoshi, T., et al. 2009, *A&A*, 494, 157
- de Wit, W. J., Hoare, M. G., Oudmaijer, R. D., & Lumsden, S. L. 2010, *A&A*, 515, A45
- de Wit, W. J., Hoare, M. G., Oudmaijer, R. D., et al. 2011, *A&A*, 526, L5
- Dorschner, J., Begemann, B., Henning, T., Jaeger, C., & Mutschke, H. 1995, *A&A*, 300, 503
- Dwek, E., Arendt, R. G., Fixsen, D. J., et al. 1997, *ApJ*, 475, 565
- Eisner, J. A., Chiang, E. I., Lane, B. F., & Akeson, R. L. 2007, *ApJ*, 657, 347
- Eisner, J. A., Hillenbrand, L. A., White, R. J., Akeson, R. L., & Sargent, A. I. 2005, *ApJ*, 623, 952
- Fontani, F., Beltrán, M. T., Brand, J., et al. 2005, *A&A*, 432, 921
- Frank, A., Ray, T. P., Cabrit, S., et al. 2014, *Protostars and Planets VI*, 451
- Fritz, T. K., Gillissen, S., Dodds-Eden, K., et al. 2011, *ApJ*, 737, 73
- Hartmann, L. 2009, *Accretion Processes in Star Formation: Second Edition* (Cambridge: Cambridge University Press)
- Jaffe, W. J. 2004, in *Society of Photo-Optical Instrumentation Engineers (SPIE) Conference Series*, Vol. 5491, *Society of Photo-Optical Instrumentation Engineers (SPIE) Conference Series*, ed. W. A. Traub, 715
- Johnston, K. G., Robitaille, T. P., Beuther, H., et al. 2015, *ArXiv e-prints*
- Kim, S.-H., Martin, P. G., & Hendry, P. D. 1994, *ApJ*, 422, 164
- Kraus, S., Calvet, N., Hartmann, L., et al. 2012, *ApJ*, 752, 11
- Kraus, S., Hofmann, K.-H., Menten, K. M., et al. 2010, *Nature*, 466, 339
- Kraus, S., Ireland, M. J., Sitko, M. L., et al. 2013, *ApJ*, 768, 80
- Kreplin, A., Kraus, S., Hofmann, K.-H., et al. 2012, *A&A*, 537, A103
- Laor, A. & Draine, B. T. 1993, *ApJ*, 402, 441
- Lee, C.-F., Mundy, L. G., Reipurth, B., Ostriker, E. C., & Stone, J. M. 2000, *ApJ*, 542, 925
- Lee, C.-F., Stone, J. M., Ostriker, E. C., & Mundy, L. G. 2001, *ApJ*, 557, 429
- Leinert, C., Graser, U., Przygodda, F., et al. 2003, *Ap&SS*, 286, 73
- Li, A. & Draine, B. T. 2001, *ApJ*, 554, 778
- Li, Z.-Y. & Shu, F. H. 1996, *ApJ*, 468, 261
- Lopez, B., Antonelli, P., Wolf, S., et al. 2008, in *Society of Photo-Optical Instrumentation Engineers (SPIE) Conference Series*, Vol. 7013, *Optical and Infrared Interferometry*, ed. M. Schöller, W. C. Danchi, & F. Delplancke
- Lutz, D. 1999, in *ESA Special Publication*, Vol. 427, *The Universe as Seen by ISO*, ed. P. Cox & M. Kessler, 623
- MacLeod, G. C., van der Walt, D. J., North, A., et al. 1998, *AJ*, 116, 2936
- Malbet, F., Lachaume, R., Berger, J.-P., et al. 2005, *A&A*, 437, 627
- Martins, F., Schaerer, D., & Hillier, D. J. 2005, *A&A*, 436, 1049
- Mathis, J. S., Rimpl, W., & Nordsieck, K. H. 1977, *ApJ*, 217, 425
- Monnier, J. D. 2007, *New A Rev.*, 51, 604
- Monnier, J. D., Tuthill, P. G., Ireland, M. J., Cohen, R., & Tannirkulam, A. 2004, in *Bulletin of the American Astronomical Society*, Vol. 36, *American Astronomical Society Meeting Abstracts*, 1367
- Persson, S. E. & Campbell, B. 1987, *AJ*, 94, 416
- Ragland, S., Ohnaka, K., Hillenbrand, L., et al. 2012, *ApJ*, 746, 126
- Scalise, Jr., E., Rodriguez, L. F., & Mendoza-Torres, E. 1989, *A&A*, 221, 105
- Stecklum, B., Caratti o Garatti, A., & Linz, H. 2012, in *Astronomical Society of the Pacific Conference Series*, Vol. 464, *Circumstellar Dynamics at High Resolution*, ed. A. C. Carciofi & T. Rivinius, 369
- Tuthill, P. G., Monnier, J. D., Danchi, W. C., Wishnow, E. H., & Haniff, C. A. 2000, *PASP*, 112, 555
- Urquhart, J. S., Busfield, A. L., Hoare, M. G., et al. 2007, *A&A*, 474, 891
- van Boekel, R. 2004, PhD thesis, FNWI: Sterrenkundig Instituut Anton Pannekoek, Postbus 19268, 1000 GG Amsterdam, The Netherlands
- Vehoff, S., Hummel, C. A., Monnier, J. D., et al. 2010, *A&A*, 520, A78
- Vural, J., Kraus, S., Kreplin, A., et al. 2014a, *ArXiv e-prints*
- Vural, J., Kreplin, A., Kishimoto, M., et al. 2014b, *A&A*, 564, A118
- Vural, J., Kreplin, A., Kraus, S., et al. 2012, *A&A*, 543, A162
- Wang, Y., Weigelt, G., Kreplin, A., et al. 2012, *A&A*, 545, L10
- Weingartner, J. C. & Draine, B. T. 2001, *ApJ*, 548, 296
- Wheelwright, H. E., de Wit, W. J., Oudmaijer, R. D., et al. 2012, *A&A*, 540, A89
- Whitney, B. A., Wood, K., Bjorkman, J. E., & Cohen, M. 2003a, *ApJ*, 598, 1079
- Whitney, B. A., Wood, K., Bjorkman, J. E., & Wolff, M. J. 2003b, *ApJ*, 591, 1049
- Wright, C. M., Siebenmorgen, R., Stecklum, B., Sterzik, M., & Käufel, H.-U. 2008, in *Society of Photo-Optical Instrumentation Engineers (SPIE) Conference Series*, Vol. 7014, *Ground-based and Airborne Instrumentation for Astronomy II*
- Xu, Y., Reid, M. J., Zheng, X. W., & Menten, K. M. 2006, *Science*, 311, 54
- Zhang, Y., Tan, J. C., & McKee, C. F. 2013, *ApJ*, 766, 86

Appendix A: Geometric fits to the K -band visibilities

In this section, we provide an updated version of Table S3 from Kraus et al. (2010). Due to an error in the program used in that work to calculate the visibilities of the temperature-gradient disk model, the outer annuli received too little weight. As a result, the fitting algorithm compensated by increasing r_{in} .

We refer to Section S4 of the work from Kraus et al. (2010) for a detailed description of the various models. As in that work, we adopt an extended component in the form of a Gaussian with a FWHM of 108 mas, which contributes 15% of the total K -band flux. We show the results of the fitting procedure in Table A.1.

We find the same results as Kraus et al. (2010) for the UD, RING and GAUSS models, which were not affected by the aforementioned error. However, for the temperature-gradient disk models, the inner radii r_{in} are significantly smaller, and the temperature gradients (described by the power-law index q) are steeper than those reported by Kraus et al. (2010).

Appendix B: Supplementary material

Table A.1. Fit parameters for geometric models to *K*-band visibilities

Model	θ [mas]	r_{in} [mas]	T_{in} [K]	q	$i^{(a)}$ [$^\circ$]	$\phi^{(b)}$ [$^\circ$]	$\chi^2_{r,V}$	$\chi^2_{r,\Phi}$	χ^2_r
UD	8.03				41	111	4.90	2.59 ^(d)	4.49
RING	5.38				40	115	6.61	2.59 ^(d)	5.89
GAUSS	5.43				45	114	2.54	2.59 ^(d)	2.55
DISK 1500 K		1.27	1500 ^(c)	0.43	46	114	1.27	2.60 ^(d)	1.51
DISK 1800 K		1.14	1800 ^(c)	0.47	46	114	1.26	2.60 ^(d)	1.49
DISK 2000 K		1.12	2000 ^(c)	0.50	46	114	1.25	2.60 ^(d)	1.48

Notes. As described in Appendix A, all models also include an extended component (Gaussian FWHM 108 mas) in order to reproduce the bispectrum speckle observations.

(a) This column gives the disk inclination, measured from the polar axis (i.e. 0° is pole-on).

(b) This column gives the model orientation, measured east of north.

(c) In the fitting procedure, this parameter was kept fixed.

(d) Given that these geometric models are point-symmetric, they predict a zero closure phase signal, resulting in the given $\chi^2_{r,\Phi}$ value.

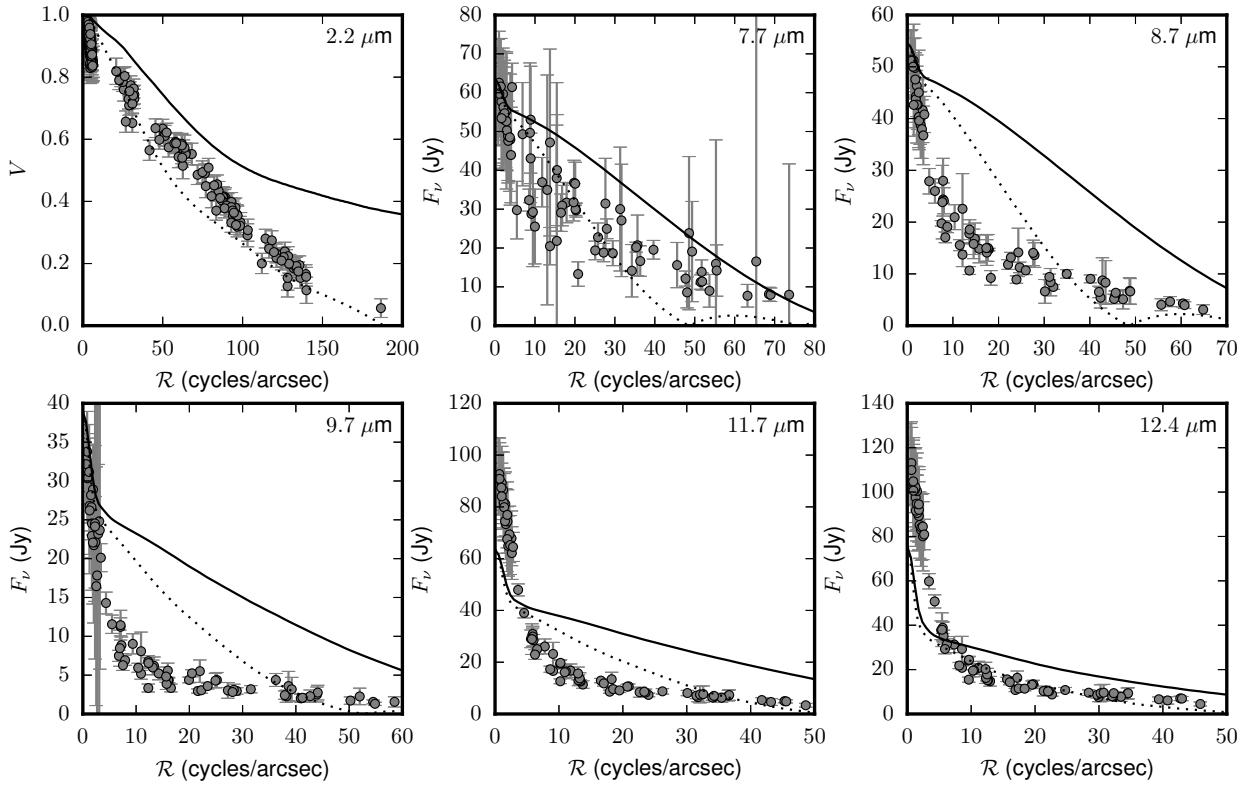


Fig. B.1. *K*-band visibilities and *N*-band correlated fluxes for the Kraus et al. (2010) model, as a function of deprojected spatial frequency. The solid and dotted lines show the model predictions perpendicular and parallel to the disk, respectively.